RSC Advances

PAPER

View Article Online
View Journal | View Issue

Cite this: *RSC Adv.*, 2025, **15**, 5681

Synthesis of Sb_2S_3:Eu thin films as a catalyst for the efficient photocatalytic degradation of rhodamine B (RhB) dye under visible light†

Adel Chihi*

Received 7th October 2024
Accepted 14th November 2024

DOI: 10.1039/d4ra07208a

rsc.li/rsc-advances

Eu was successfully incorporated into Sb_2S_3 thin films for proficient photocatalytic degradation of rhodamine B (RhB) dye under visible light. In this work, we reported the effect of incorporating Eu ions into Sb_2S_3 thin films at different doping levels to tailor their structural, optical, electrical, and photocatalytic properties. Grazing incidence X-ray diffraction (GIXRD) analysis revealed that the fabricated films exhibited an orthorhombic crystalline structure. Additionally, the GIXRD peaks shifted towards lower angles as the doping level increased. The Williamson–Hall method was used to estimate the effective crystallite size considering the strain components. The field emission scanning electron microscope (FESEM) characterisation demonstrated that the grain size decreased and a denser microstructure was observed as the Eu degree increased. The estimated optical band gap (E_g) value increases from 1.67 eV to 1.72 eV as the level of Eu doping rises from 0 to 8 at%, making the films suitable for photocatalytic applications. The photocatalytic activities of the pristine and Eu-doped Sb_2S_3 thin films were evaluated by the degradation of highly toxic Rhodamine B (RhB) dye under dark and various light conditions for 120 min. A remarkable photodegradation rate was achieved with the optimal doping level of 4 at% of Eu, demonstrating a 90.99% degradation of RhB. Electrochemical impedance spectroscopy (EIS) measurements show that the lifespan of photoinduced electrons for 4 at% Eu^{3+} samples is approximately 10 fold higher than that of the pristine sample. In terms of chemical kinetics, the degradation of RhB by the Sb_2S_3:Eu (4 at% of Eu) photocatalyst was found to follow pseudo-first-order kinetics with a rate constant of 0.049 min^{-1} under visible light irradiation. A conceivable molecular mechanism for photocatalytic degradation of the RhB dye by Sb_2S_3:Eu photocatalysts is also provided. These results highlight the potential of Eu-doped Sb_2S_3 thin films for advanced photocatalytic applications. Specifically, Sb_2S_3:Eu 4 at% exhibits favourable properties. Thus, it was concluded that these photocatalysts are highly suitable for the remediation of dye-contaminated wastewater.

1. Introduction

The growth in semiconductor research and its impact on photocatalytic applications for removing pollutants in water has surged noticeably. Pollutants with high solubility and chemical stability represent a primary environmental challenge, posing significant risks to ecosystems and human health. This use of semiconductors in photocatalysis has become prevalent for addressing environmental concerns and safeguarding human health from the harmful effects of pollutants. By harnessing the photocatalytic properties of semiconductors, researchers aim to develop efficient and sustainable methods for degrading organic contaminants, thereby modifying their adverse impacts on the environment and public health. Chalcogenide semiconductors, including antimony sulfide (Sb_2S_3), antimony selenide (Sb_2Se_3), and $Cu_2ZnSn(S, Se)_4$, are emerging as promising photocatalysts for removing organic pollutants from wastewater.[1–5] Among the various chalcogenide semiconductors, Sb_2S_3 has been typically studied due to its superior physical and chemical properties. Sb_2S_3 is a significant V–VI semiconductor with a high absorption coefficient of 10^4–10^5 cm^{-1} in the visible region,[6] optical band gap ranging from 1.5 to 1.7 eV (ref. 7) and overwhelming air/moisture-stability.[8] Its use as a light-harvesting material in tandem solar cells,[9,10] and one-dimension (1D) parallel nanoribbon grain structure $(Sb_4S_6)_n$ where atoms are covalently bonded along the [001] crystallographic direction[11,12] has attracted large scientific interest. Unfortunately, these advantages are accompanied by high electron–hole (e^-/h^+) pair recombination and significant electrical resistivity,[11,13] which hinders using pristine Sb_2S_3 as a photocatalyst.

To address the high recombination rate of e^-/h^+ pairs and electrical resistivity, various strategies were explored to overcome

---

Photovoltaic Laboratory, Research and Technology Centre of Energy, Borj-Cedria Science, and Technology Park, BP 95, 2050 Hammam Lif, Tunisia. E-mail: adel.chihi@crten.rnrt.tn; Fax: +216 79325825; Tel: +216 54350506

† Electronic supplementary information (ESI) available. See DOI: https://doi.org/10.1039/d4ra07208a

the efficiency bottleneck in the photocatalytic degradation of organic pollutants using the Sb_2S_3 photocatalyst. Among the strategies, doping is indeed a widely recognized strategy to improve the photocatalytic efficiency of semiconductor photocatalysts. By introducing foreign atoms or ions into the semiconductor's crystal lattice, doping can adjust the electronic structure and create new energy states within the band structure, facilitating the separation and transport of photoexcited charge carriers. These trapped charges can then migrate to the surface of the photocatalyst, where they participate in redox reactions with adsorbed pollutant molecules, ultimately leading to their degradation. This mechanism effectively reduces the recombination of e^-/h^+ pairs and enhances the overall photocatalytic activity of the material.[14] Doping Sb_2S_3 material with an appropriate chemical element such as Bi,[15] Ru,[16] Sn,[17] and O,[12] and so on is an effective and reasonable strategy for enhancing the efficiency of photocatalytic reactions, reducing e^-/h^+ recombination processes, and boosting electrical conductivity. However, this strategy requires further investigation, as the availability of rare earth (RE) elements remains complex and poses environmental challenges. RE dopants have emerged as highly effective materials by acting as trapping sites, reducing the recombination process and extending the mean lifetime of charge carriers.[18] According to research conducted by Liu *et al.*, epitaxially grown Sb_2S_3:Tm^{3+} nanorods improve the carrier transportation efficiency of Sb_2S_3 and inhibit carrier recombination. This, in turn, creates a stronger driving force to optimize the interfacial transport of carriers.[19] Moreover, they demonstrated that the photocurrent density (-0.91 mA cm^{-2}) is improved about 18 times compared to the pristine Sb_2S_3 photocathode. Despite existing studies on the impact of RE doping on photocatalysis, discussions in this field have generally been superficial, underscoring a clear need for more in-depth exploration. Among RE ions, Eu^{3+} is one of the most studied, due to its negligible toxicity and optical properties.[20] Therefore, engineered Eu-doped Sb_2S_3 is of interest for photocatalytic applications since it can absorb visible light, improve charge carrier separation, tailor physicochemical properties, and offer cost-effectiveness. As far as we know, no previous research has investigated the impact of Sb_2S_3:Eu thin films on the photocatalytic degradation of RhB dyes.

In this work, we have investigated the effect of Eu doping on the physicochemical properties of the Sb_2S_3 thin film using various techniques including GIXRD, SEM, EDX, UV-visible spectroscopy, Hall effect, and electrochemical impedance spectroscopy to understand how the doping influences the structural, morphological, optical, and electric characteristics of the Sb_2S_3 material. These physicochemical properties are crucial for the catalytic activity of the Sb_2S_3 thin film, aiming to enhance its photocatalytic performance in the visible region. The photocatalytic activity of the Eu-doped Sb_2S_3 photocatalyst was assessed by Rhodamine B (RhB) degradation under visible light irradiation. The degradation experiments of RhB on the synthesized Eu-doped Sb_2S_3 thin film were carried out to determine adsorption kinetics. In addition, the photocatalytic mechanism elucidated by scavenger studies revealed that $^{\bullet}OH$ and $^{\bullet}O_2^-$ were the primary reactive radicals responsible for the degradation process.

1.1 Materials

Antimony(III) chloride $SbCl_3$ (99.9%, Merck & Co. Inc), 2-methoxy ethanol $C_3H_8O_2$ (99.8%, Fisher Scientific Inc.), ethanolamine C_2H_7NO (≥98%, Sigma-Aldrich Co), and thiourea CH_4N_2S (≥99%, Sigma-Aldrich Co) were chemicals compounds used for the synthesis of Sb_2S_3 precursors and thin films. Europium nitrate pentahydrate $Eu(NO_3)_3 \times 5H_2O$ (99.9%, Sigma-Aldrich Co). Rhodamine B (RhB) $C_{28}H_{31}ClN_2O_3$ (≥95, Sigma-Aldrich Co). Acetic acid (≥99.7%, Sigma-Aldrich Co), ethanol (≥99.8%, Sigma-Aldrich Co), and de-ionized (DI) water of 18 MΩ cm resistivity were used in the preparation of solutions and for rinsing of the samples. Isopropanol (IPA), ethylenediaminetetraacetic acid (EDTA), potassium dichromate (K_2CrO_7), and *p*-benzoquinone (*p*-BQ) were used for the identification of radical species. Quartz glass plates were purchased from Sigma-Aldrich. The chemicals employed in the experiment were utilised without additional purification unless explicitly mentioned otherwise in the experimental procedures.

1.2 Material synthesis

Firstly, 1.5 g of antimony(III) chloride was dissolved in 30 mL of 2-methoxy ethanol on a magnetic stirrer for 15 min. Then, 60 drops of ethanolamine were added as a stabiliser. Afterwards, 0.75 g of thiourea was added to this solution and stirred for a minimum of 1 h under ambient conditions to form a homogeneous solution. The mixed solution was ultrasonicated for 24 hours at room temperature. To produce Eu-doped Sb_2S_3 films, an aqueous solution of different molar ratios of europium nitrate pentahydrate/antimony(III) chloride (2, 4, 6, and 8 at%) was prepared and slowly added dropwise in the first solution. Before the experiments, the quartz glass substrates were thoroughly ultrasonically cleaned with ethanol, and deionised water (DI) for 20 min. Then, the substrate was dried in an oven at 100 °C. Next, the glass substrates were dip-coated with the prepared solution using a dip coater on an anti-vibration platform. Subsequently, the glass substrates were immersed into the prepared solution at a speed of 5 mm min^{-1}, followed by a dwell time of 30 s. Next, the substrates were withdrawn at a fixed speed of 100 mm min^{-1} and allowed to dry overnight in a storage box before the characterisation steps. Then, the surface compatibility between the glass substrate and the solution was assessed through contact angle measurements, where a lower contact angle indicates enhanced wettability and compatibility. The synthesized films were subjected to thermal annealing at an optimized temperature of 300 °C for 5 min. The annealing process was carried out under argon gas using rapid thermal processing (RTP) with infrared (IR) heating lamps to minimize sulfur depletion from the samples. Lastly, the samples were cooled to room temperature for subsequent activity experiments and characterizations. The thickness of the obtained Eu-doped Sb_2S_3 films is about 500 nm measured using a Bruker Dektak XT contact profilometer.

1.3 Characterization measurements

The morphology of the deposited films was characterized using a field emission scanning electron microscope (FE-SEM) ZEISS

SUPRA 55 VP. In addition, the chemical composition of the synthesized films was determined by energy-dispersive X-ray spectroscopy (EDS). The crystalline structure and phase purity of pristine and Sb_2S_3:Eu films were assessed through grazing incidence X-ray diffraction at 0.5° (GIXRD, PANalytical X'Pert Pro system) with a monochromatic CuK_α radiation source ($\lambda = 1.5406$ Å). A comparison was made with the Joint Committee on Powder Diffraction Standards (JCPDS) card to identify the detected peaks, and a triplet of Miller indices was associated with each peak. Raman scattering spectroscopy was carried out on all synthesized samples using a Jobin Yvon LabRAM HR spectrometer with a He–Ne laser source (632.81 nm). The samples were subsequently analysed using UV/Vis spectroscopy (Ultraviolet-Visible Spectroscopy) with a UV visible-NIR LAMBDA 950 spectrophotometer in the wavelength window between 600 nm and 1200 nm at room temperature. Electrochemical Impedance Spectroscopy (EIS) was carried out to fix the charge transfer resistance and other key parameters of the electrochemical system in the presence of solar light in the frequency range between 1 MHz to 10 mHz with an AC amplitude of 10 mV at an open circuit bias. Lastly, Hall effect measurements using the Van der Pauw technique under a constant magnetic field of small magnitude ($B = 0.5$ T) applied perpendicular to the plane of the film and current ($I = 1.5$ mA) were conducted to investigate the electrical properties of the deposited Sb_2S_3 thin films. These measurements were performed with a conventional four-probe technique at room temperature using the HMS-3000 instrument.

1.4 Photocatalytic activity measurement

The photocatalytic activity of all Sb_2S_3 thin-film photocatalysts was evaluated by measuring the degradation of RhB aqueous solution. The RhB dye was dissolved in a 100 mL beaker containing DI water to achieve a concentration of 10 mg. L^{-1}. All the synthesised thin films with a surface of 1 × 1 cm^2 were submerged in RhB aqueous solutions within a separate 20 mL glass beaker. Then, All the solutions were magnetically stirred in the dark for 30 minutes to ensure equilibrium between the adsorption and desorption of the dye on the surface of the photocatalysts. The RhB concentration after adsorption equilibrium pretended as the initial concentration C_0. The degradation experiments were conducted under a 300 W xenon lamp equipped with a cutoff filter ($\lambda \geq 420$ nm) as a light source for 120 min which was located vertically at the prepared solutions. The beaker containing the reaction mixture was about 10 cm from the xenon lamp. During the experiment, 5 mL of the degraded solution was withdrawn approximately every 20 min and analysed at $\lambda_{max} = 554$ nm using a PerkinElmer Lambda 950 spectrophotometer to estimate RhB decomposition. The photoactivity efficiency and the amounts of degraded dye can be estimated using the following equations:

$$\text{Degraded efficiency}(\%) = \left(1 - \frac{C_t}{C_0}\right) \times 100 \tag{1}$$

$$q = \frac{V}{m}(C_0 - C_t) \tag{2}$$

where C_0 and C_t represent the initial concentration before the reaction and the remaining concentrations of RhB at each time, all the photocatalytic performances were tested under UV light, visible light, and sunlight. V is the volume of dye solution (L); m is the mass of adsorbent (g). The temperature remained constant at about 25 °C during the experimental runs.

To investigate the stability of the photocatalysts, the deposited films were reused five times for the photocatalytic degradation of RhB (10 mg L^{-1}). Furthermore, the active radical trapping experiment followed the same procedure as the degradation experiment, with the addition of specific scavenging agents to selectively target different radicals. The trapping experiment conditions involved adding 2 mL of scavenger solution to the aqueous phase, including 1 mM *p*-BQ for scavenging superoxide radicals ($^{\bullet}O_2^{-}$), 5 mM IPA for hydroxyl radicals ($^{\bullet}OH$), 5 mM EDTA for holes (h^+), and 5 mM K_2CrO_7 for electrons (e^-). The influence of each scavenger on the degradation process was evaluated against the process without scavengers.

2. Results and discussion

2.1 Structural analysis

The crystallographic characteristics of pristine and Eu-doped Sb_2S_3 films deposited on a quartz glass substrate are investigated by GIXRD as shown in Fig. 1. All the diffraction peaks are well indexed to the orthorhombic crystal structure of stibnite Sb_2S_3 (ref. 21) (JCPDS card no: 42-1393 with lattice constants $a = 11.310$ Å, $b = 3.836$ Å, $c = 11.228$ Å and *Pbnm* space group symmetry) with a prominent peak positioned at Bragg angle of 29.3° corresponding to (221) plane. This result of the preferred orientation of Sb_2S_3 is in line with the findings of other earlier studies.[15] Regarding the detection limit of the GIXRD technique, no evidence of Eu_2O_3 or other crystal phases such as Sb or Sb_2O_3 impurities has been detected in the GIXRD pattern, corroborating that Eu^{3+} ions are integrated into the Sb_2S_3 host lattice. Nevertheless, scrupulous analysis of Fig. 1(a) delineates that the preferred diffraction peak matching to the (221) plane of Eu-doped Sb_2S_3 slightly shifts to the left compared to the pristine one, indicating that the crystal structure is shrinking with the rise in the Eu^{3+} doping. The shifting of the high-intensity GIXRD peak is shown in the magnified region of the GIXRD pattern with 2θ ranging from 28.5° to 30° (Fig. 1(b)). The shifting generated herein is attributed to the larger ionic radii of Eu^{3+} ions (with a radius of 0.95 Å)[22,23] compared to Sb^{3+} ions (with a radius of 0.76 Å).[24] X. Liu *et al.* found the same effect when doping Sb_2S_3 thin films with Tm^{3+} ions.[19] The maximum shift of approximately 0.17° was detected at an Eu doping level of 8 at%. There is also a decrease in intensity with increased Eu^{3+} doping levels. This behaviour could be due to an increase in the arrangement of the atoms inside the Sb_2S_3 host lattice. On the other hand, the strain effect can be quantified using the Williamson–Hall (W–H) method.[25] This approach helps to separate the contributions of crystallite size and lattice strain to the broadening of the GIXRD peaks. The effective crystallite size (D) and lattice microstrain (ε) were estimated using the following equation:

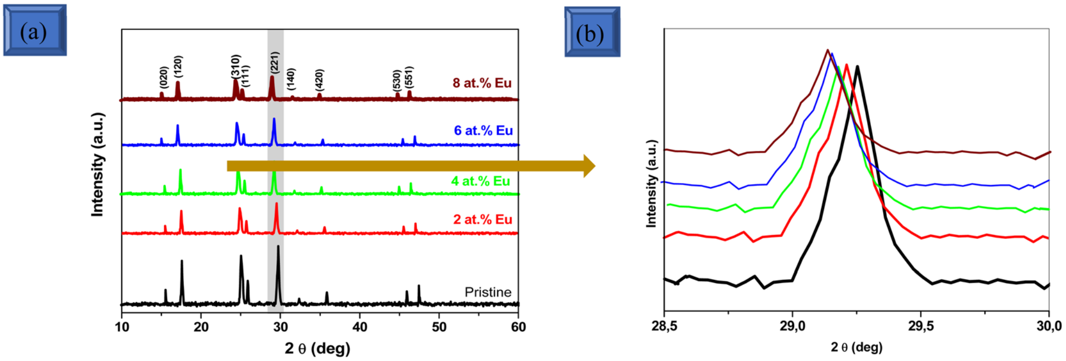

Fig. 1 (a) GIXRD patterns of pristine and Eu-doped Sb_2S_3 films at various doping levels. (b) A zoomed-in view of the (221) peak in the 2θ range of 28.5–30° for both pristine and Eu-doped Sb_2S_3 films, showing the impact of doping on the main peak position.

$$\beta_{hkl}\cos\theta = \frac{K\lambda}{D} + 4\varepsilon\sin\theta \tag{3}$$

where K is a dimensionless shape factor, with a typical value of 0.94 for spherical crystallites; λ is the wavelength of the X-ray radiation (1.5418 Å), ε is the mean value of internal microstrain, while β_{hkl} (rad) and θ are the full width at half maximum (FWHM) and Bragg's angle, respectively.

Using Origin software, we plotted $\beta_{hkl}\cos(\theta)$ *versus* $4\sin(\theta)$. The intercept on the y-axis of this plot gives the effective crystallite size, while the ε was obtained from the slope of the linear fit to the experimental data. Using this method, the effective crystallite size and microstrain can be accurately determined, providing more detailed insight into the effect of Eu^{3+} ions doping on the crystal lattice of the material. As seen from Fig. 2, a positive slope for all the samples reveals the presence of tensile strain, leading to an increase in lattice parameters disclosed through the left shift of the observed peaks from the GIXRD pattern. The lattice strain in the Sb_2S_3 crystalline structure results from two surface strains arising from grain size and localised strain due to numerous sulfur vacancies. As we know, the GIXRD peaks shift to lower angles with tensile stress whereas the GIXRD peaks shift toward higher angles with compressive stress.[26] The crystallite size and microstrain for different doping levels are gathered in Table 1. It has been observed that the crystallite size obtained using the W–H expression reduced with the rise of the Eu dopant amount. The average crystallite size of all the Sb_2S_3 films varies from 35 nm to 18 nm. This can be ascribed to lattice strain's appearance and doping-induced defects. Nevertheless, the microstrain increases as the doping level increases and reaches its maximum value of about 2.17×10^{-4} for the sample doping with 8 at% of Eu. This increase in microstrain with higher doping levels could be attributed to multiplied defects and GBs resulting from the decreased grain size.[27] The lattice parameters for Sb_2S_3 films with orthorhombic structure were estimated using the following equations:[28]

$$\frac{1}{{d_{hkl}}^2} = \frac{h^2}{a^2} + \frac{k^2}{b^2} + \frac{l^2}{c^2}, \tag{4}$$

$$2d_{hkl}\sin\theta = n\lambda \tag{5}$$

where d_{hkl} represents the inter-plane spacing, h, k, and are the Miller indices, while a, b, c denotes the lattice parameters. Table 1 presents the lattice constants of the pristine and Eu-doped Sb_2S_3 films at various doping levels. Significant alteration was detected in the lattice parameters with varying doping levels. The lattice parameters a, b, and c were changed to $a = 11.339$ Å, $b = 3.857$ Å, and $c = 11.252$ Å when 4 at% Eu doping level was applied into stibnite Sb_2S_3, which led to an expansion of about 1.4% in the volume of the unit cell. Doping with Eu atoms increased the lattice parameters a, b, and c of the orthorhombic crystal structure of Sb_2S_3, indicating that Eu has likely incorporated into the Sb_2S_3 host lattice. As we know, substitutional doping occurs when the level of the dopant is below the solubility limit; however, interstitial doping is more common when the doping level exceeds the solubility limit, creating a new crystal structure. Bragg's law led us to conclude that the downshift would result in a greater inter-spacing between the (221) crystal planes of the Sb_2S_3 lattice. Hence, the smaller 2θ value of the (221) corresponds to the greater spacing $d_{(221)}$ in the distorted Sb_2S_3 crystals. To summarise, there were differences in the lattice parameters between pristine and Eu-doped Sb_2S_3 thin film, suggesting that Eu^{3+} incorporated into the lattice of Sb_2S_3 and substituted the Sb^{3+} ions. This substitution would eventually be beneficial for splitting the charge carriers, enlarging their lifetime, and effectively hindering the recombination of e^-/h^+ pairs.

2.2 Raman spectroscopy study

A Raman spectroscopy was used to investigate the changes in vibrational modes and lattice structural characteristics of Sb_2S_3 as a function of Eu doping. Raman spectroscopy is a non-destructive technique that provides information about molecular vibrations, phonon modes, and local atomic arrangements. This technique is an imperative complement to GIXRD measurement for thorough material characterisation since it is sensitive to bonding and local symmetry variation. Theoretically, there are 30 Raman active optical phonon modes of Sb_2S_3 at the Γ point of the Brillouin zone[29] (Table S1†):

$$\Gamma_{\text{Raman}} = 10A_g \oplus 5B_{1g} \oplus 10B_{2g} \oplus 5B_{3g} \tag{6}$$

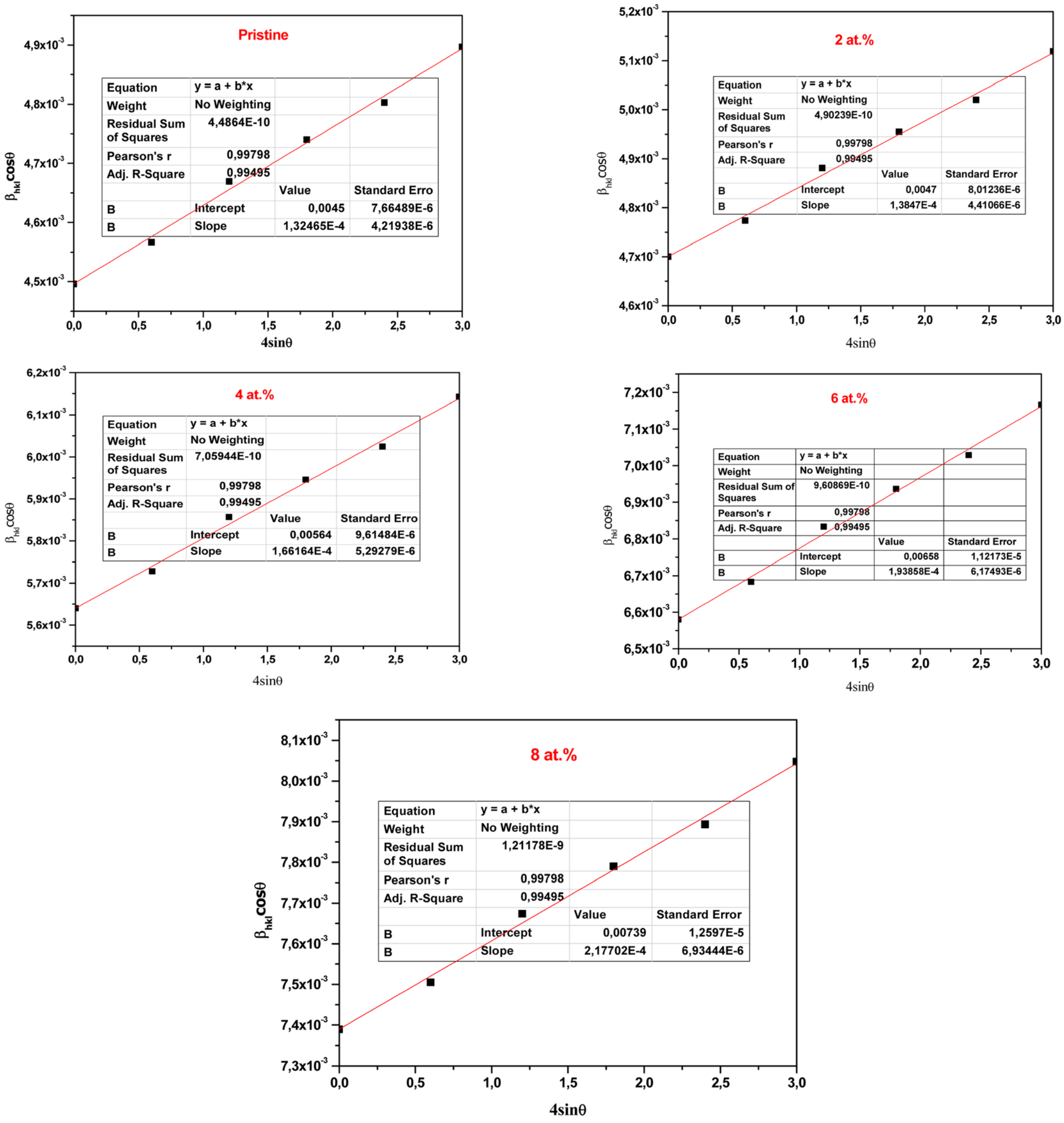

Pristine

Equation	y = a + b*x		
Weight	No Weighting		
Residual Sum of Squares	4,4864E-10		
Pearson's r	0,99798		
Adj. R-Square	0,99495		
		Value	Standard Erro
B	Intercept	0,0045	7,66489E-6
B	Slope	1,32465E-4	4,21938E-6

2 at.%

Equation	y = a + b*x		
Weight	No Weighting		
Residual Sum of Squares	4,90239E-10		
Pearson's r	0,99798		
Adj. R-Square	0,99495		
		Value	Standard Error
B	Intercept	0,0047	8,01236E-6
B	Slope	1,3847E-4	4,41066E-6

4 at.%

Equation	y = a + b*x		
Weight	No Weighting		
Residual Sum of Squares	7,05944E-10		
Pearson's r	0,99798		
Adj. R-Square	0,99495		
		Value	Standard Erro
B	Intercept	0,00564	9,61484E-6
B	Slope	1,66164E-4	5,29279E-6

6 at.%

Equation	y = a + b*x		
Weight	No Weighting		
Residual Sum of Squares	9,60869E-10		
Pearson's r	0,99798		
Adj. R-Square	0,99495		
		Value	Standard Error
B	Intercept	0,00658	1,12173E-5
B	Slope	1,93858E-4	6,17493E-6

8 at.%

Equation	y = a + b*x		
Weight	No Weighting		
Residual Sum of Squares	1,21178E-9		
Pearson's r	0,99798		
Adj. R-Square	0,99495		
		Value	Standard Error
B	Intercept	0,00739	1,2597E-5
B	Slope	2,17702E-4	6,93444E-6

Fig. 2 Williamson–Hall (WH) plot for the pristine and Eu-doped Sb_2S_3 films at different doping levels.

Table 1 Structural parameters of pristine and Eu-doped Sb_2S_3 films at various doping levels from GIXRD patterns

Sample	Crystallite size (nm)	Lattice strain (ε)	Lattice parameters (Å)		
			a	*b*	*c*
0 at%	35	1.31×10^{-4}	11.315	3.839	11.230
2 at%	27	1.62×10^{-4}	11.324	3.846	11.238
4 at%	22	1.85×10^{-4}	11.330	3.849	11.241
6 at%	20	2.01×10^{-4}	11.339	3.857	11.252
8 at%	18	2.17×10^{-4}	11.341	3.860	11.254

where A_g and B_g represent the different symmetry species of the vibrational modes, these wide ranges of Raman modes can reveal intricate details about the material's local structural and electrical surroundings. Nonetheless, only 20 of the 30 theoretically predicted peaks have been observed experimentally.[30]

In the present work, only five Raman peaks were recorded for pristine Sb_2S_3 and Eu-doped Sb_2S_3, measured at room temperature from 100 to 350 cm^{-1} under 632.81 nm laser light excitation. This limited observation is possibly due to accidental degeneracy or insufficient intensities caused by the small polarizability of some of the vibrations, as depicted in Fig. 3. The observed five characteristic peaks at 312, 285, 240, 194, and 150 cm^{-1} are attributed to the vibrational modes of the stibnite phase. These peaks are consistent with the theoretically expected A_g (at 151 cm^{-1}, 282 cm^{-1}, 310 cm^{-1}), B_{1g}/B_{3g} (at 240 cm^{-1}), and B_{2g} (at 192 cm^{-1}) optical modes.[31] The Raman peaks located at about 282 and 310 cm^{-1} are usually ascribed to the symmetric vibration of the Sb_2S_3 pyramidal units with C_{3v} symmetry[32] while the Raman peaks situated at about 194 and 240 cm^{-1} are typically assigned to the Sb_2S_3 phase.[33] The obtained Raman spectra agree well with other existing studies.[34] Notably, the Raman peaks do not indicate the presence of the Sb_2O_3 phases for all the samples, which confirms the GIXRD

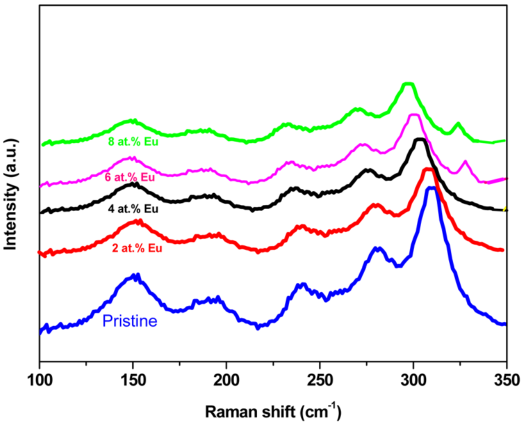

Fig. 3 Raman spectra of pristine and Eu-doped Sb_2S_3 films at different doping levels, illustrating the effects of Eu doping on the vibrational modes of the Sb_2S_3 thin films.

results. However, beyond the doping level of 4 at%, a weak Raman peak was detected at about 338 cm^{-1}, usually ascribed to the F_g mode of Eu_2O_3.[35] This fact can occur if Sb^{3+} ions are substituted by Eu^{3+} in the Sb_2S_3 host lattice at a low doping level (<4 at%) and are placed in interstitial positions at a higher doping level. The Eu^{3+} ions have a higher possibility of occupying Sb^{3+} sites. However, when these sites saturate at 4 at%, the Eu^{3+} ions are located interstitially. This unexpected outcome is slightly unsettling for the effectiveness of photocatalysis, as this phase Eu_2O_3 is traditionally seen as a cluster for e^-/h^+ pairs recombination.[36] This discrepancy between GIXRD and Raman results arises since they probe different aspects of the material's structure. GIXRD is focused on the Sb_2S_3 crystal lattice and long-range order, while Raman spectroscopy is focused on molecular vibrations and local chemical environments. These outcomes showed that the small quantity of Eu (≤4 at%) that substituted Sb could keep the crystallinity of the Sb_2S_3 film; however, the higher Eu content (>4 at%) could induce lattice distortion and weaken the film's crystallinity, which would increase the segregation of Eu^{3+} ions in the grain boundaries (GBs). These results show that an optimal Eu doping level preserves the crystallinity of Sb_2S_3 films and significantly influences the transport properties of the photo-generated electrons and holes to the film surface and the optical bandgap, impacting the photocatalytic performance. Compared to pristine Sb_2S_3 films, the Raman peaks of Eu-doped Sb_2S_3 films exhibit a redshift, *i.e.*, shift towards the lower wavenumber by 12 cm^{-1} for all the Raman peaks with the increase of Eu doping level. The down-shift of the peak position could be attributed to changes in phonon relaxation with particle size, defects, and phonon confinement.[37,38] Consequently, optimal doping seems crucial for forming Sb_2S_3 films with good structural quality. On the other hand, the peak intensity of the phonon mode of the Eu-doped Sb_2S_3 decreases, accompanied by broadening of the FWHM of the vibrational Raman peaks, as shown in Fig. 4. This can be attributed to poor crystallinity, soft structural defects caused by doping elements with a larger ionic radius, and mechanical strain.

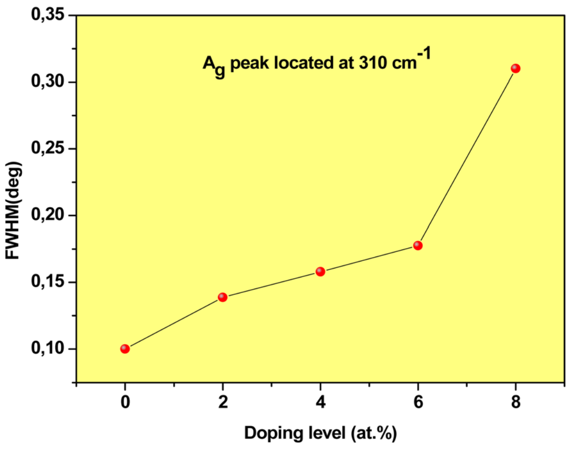

Fig. 4 The full width at half maximum (FWHM) of the main Raman peak as a function of Eu doping, showing the influence of doping on peak broadening.

2.3 Morphological and compositional analysis

SEM analysis provides essential information about the surface morphology, size, and texture of the synthesized Sb_2S_3 films on quartz glass substrates, which plays a crucial role in enhancing the quality of films and photocatalytic activity. As presented in Fig. 5, the morphology of the pristine Sb_2S_3 film exhibited inhomogenous, randomly distributed agglomerated grains of varying sizes having some voids between them. It is also worthwhile to note that the voids and shape irregularities observed in the Eu-doped Sb_2S_3 films have been significantly increased compared to pristine thin films. In addition, upon the incorporation of Eu dopant, SEM micrographs clearly show a reduction in grain size from 85 nm to 64 nm as the doping level increases from 0 at% to 8 at%, which is consistent with the GIXRD results. Fig. 6 displays the gain size histograms for pristine, and Eu-doped Sb_2S_3 films, created using ImageJ software.[39] The corresponding average grain size of the Sb_2S_3 films is exhibited in Table 2. It should be noted that the average grain size of the Sb_2S_3 films obtained by SEM analysis is larger than the crystallite size value assessed by the W–H method. This discrepancy in the crystallite size can arise for several reasons. One reason is the nature of the material: crystallite size estimated by GIXRD is influenced by crystalline order, while SEM can capture surface effects and agglomeration that may affect the apparent size. The distribution of elements was studied using EDS measurements to analyze the formation of Sb_2S_3 at different doping levels, as shown in Fig. 7. The pristine sample reveals the presence of sulfur and antimony elements with atomic percentages of 58.2% and 41.8%, respectively, confirming the formation of impurity-free pure Sb_2S_3 films. The presence of carbon is undoubtedly due to the use of thiourea as a precursor in the synthesis process. Likewise, Eu-doped samples reflect the existence of Eu elements in the EDS spectra and also do not contain any impurity elements showing the high quality of synthesized samples.

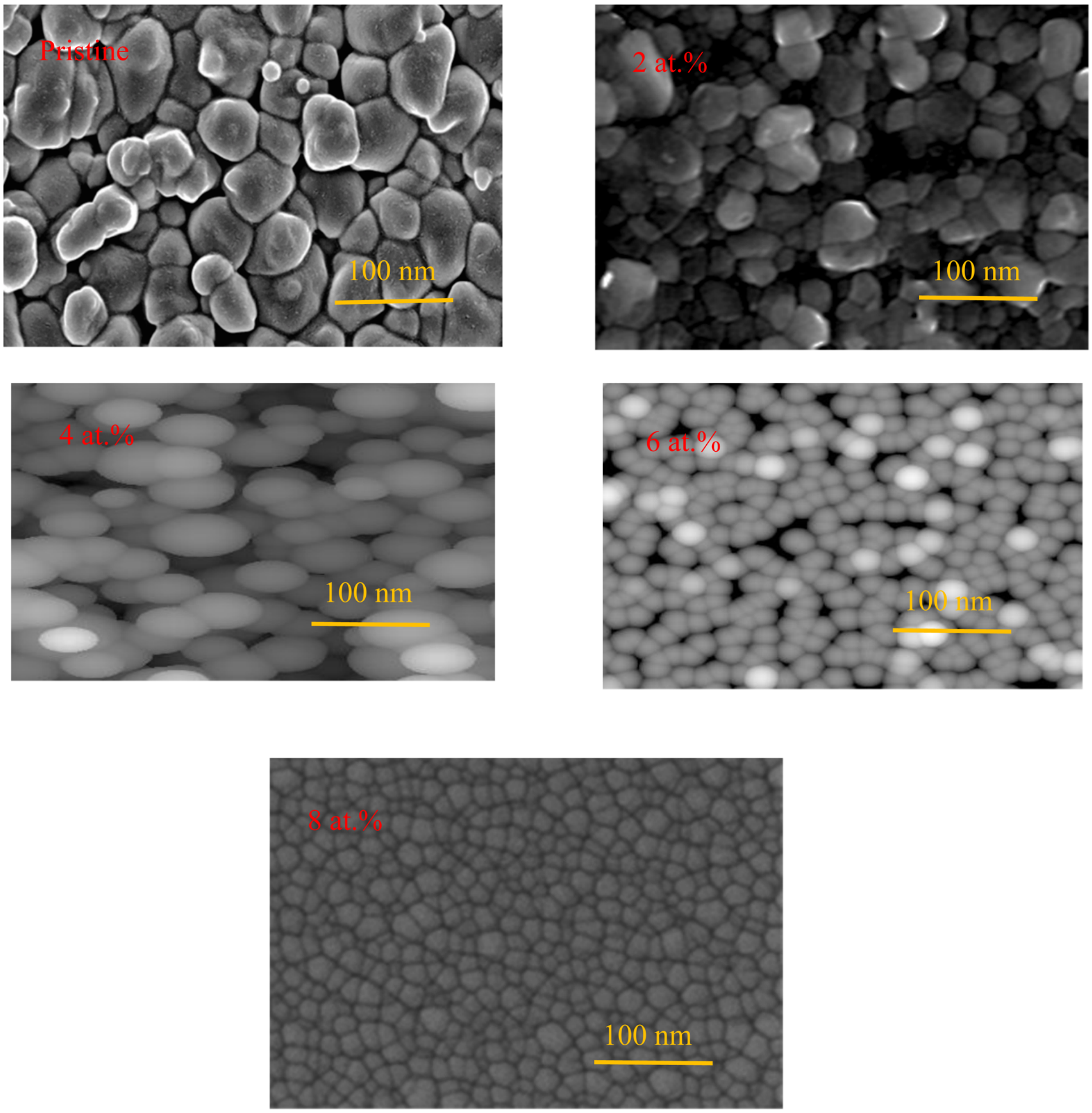

Fig. 5 The morphological micrographs of Sb_2S_3 thin films as a function of Eu content.

2.4 Optical properties

UV-vis spectroscopy was performed for all the samples deposited on a glass substrate to investigate the impact of Eu doping on the optical properties. As illustrated in Fig. 8(a and b), Eu doping affects the transmission $T(\lambda)$ and reflectivity $R(\lambda)$ spectra of Sb_2S_3 films in the wavelength window between 600 and 1200 nm. The presence of interference fringes in the transmittance and the reflectivity spectra confirms the homogeneity of the prepared films. The pristine and Eu-doped Sb_2S_3 films exhibited 60% and 80% transmittance in the visible domains, respectively, while their reflectivity was less than 20%. It is worth noting that the onset of absorption was found at 730 nm, which is in good agreement with the previously reported onset absorption edge of Sb_2S_3.[40,41] The linear optical absorption coefficient $\alpha(\lambda)$ was estimated from the transmittance and the reflectance spectra in the strong absorption region and achieved by the well-known equation:

$$\alpha(\lambda) = \frac{1}{d}\ln\left(\frac{(1-R)^2 + \left((1-R)^4 + 4R^2T^2\right)^{\frac{1}{2}}}{2\ T}\right) \tag{7}$$

where d is the thickness of the deposited films, R and T are the reflectance and transmittance, respectively.

For direct band gap semiconductors, the optical band gap can be estimated from the Tauc formula given by:

$$(\alpha h\nu) = A(h\nu - E_g)^{\frac{1}{2}} \tag{8}$$

where α, A, h, ν, and E_g stand for absorption coefficient, a constant parameter, Planck's constant, the frequency of incident light, and the optical band gap energy.[3]

The Tauc plot for all the films is shown in Fig. 9. E_g was extracted by extrapolating a straight line of $(\alpha h\nu)^2$ to zero absorption coefficient. The estimated optical band gap for

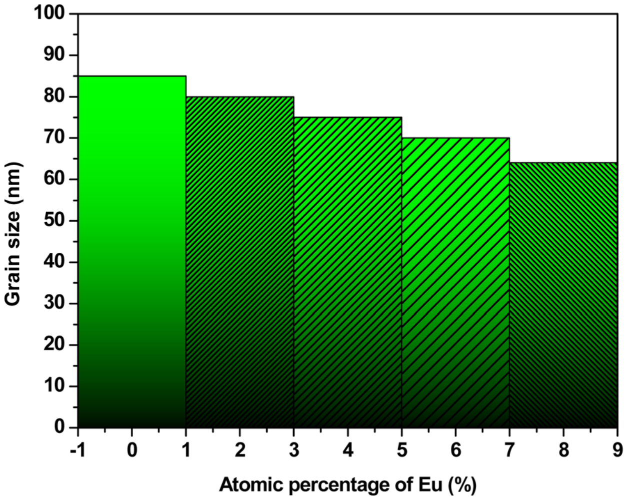

Fig. 6 The evolution of the grain size of Sb_2S_3 thin films as a function of Eu content.

Table 2 The Effect of Eu doping on the grain size of Sb_2S_3 films using ImageJ software

Sample	Pristine Sb_2S_3	2 at% Eu	4 at% Eu	8 at% Eu	8 at% Eu
Grain size (nm)	85	80	76	70	65

pristine was 1.67 eV. When Eu doping was applied up to 8 at% of Eu, the optical band gap of the pristine film progressively increased to 1.72 eV. Thus, it can be inferred that doping engineering can tune the band gap of a Sb_2S_3 semiconductor. The blue shift of the optical bandgap can be attributed to several factors, including quantum confinement, and structural elements such as crystallite size and microstrain. We believe the reduction in average crystallite size may increase defects owing to Eu ions doping. As a result, instead of the commonly observed electronic transitions from the filled valence band to the empty conduction band, these defects cause electronic transitions from the filled valence band to the defect energy levels. The incorporation of Eu^{3+} ions within the lattice of other semiconductors leads to a broadening of their optical band gap that was previously reported.[42]

It is known that the catalytic activity of a photocatalyst is closely correlated to the band gap energy. The optical band gap exhibited by the pristine and Eu-doped Sb_2S_3 films indicates their potential as effective photocatalysts, as they can absorb photons in the visible range efficiently. Nevertheless, since the band gaps of all the synthesized materials are nearly identical, a sample's superiority in photocatalytic applications cannot be attributed solely to its band gap. Particle size, phase purity, surface morphology, and the ability to suppress electron–hole (e^-/h^+) recombination are crucial factors in determining a material's photocatalytic activity.

2.5 Electrochemical impedance spectroscopy measurements

EIS analyses were conducted in a frequency window between 10 mHz and 1 MHz under illumination conditions to understand the samples' charge separation and transfer properties. The conductivity and charge transfer resistance (R_{ct}) for all the samples are assessed through the analysis of the Nyquist plot, as shown in Fig. 10(a). The semicircle, resulting from the parallel electrical circuit of resistance and capacitance, reflects the electrode surface's reaction rate, confirming a single charge transfer mechanism across the Sb_2S_3/Na_2SO_4 interface. Using

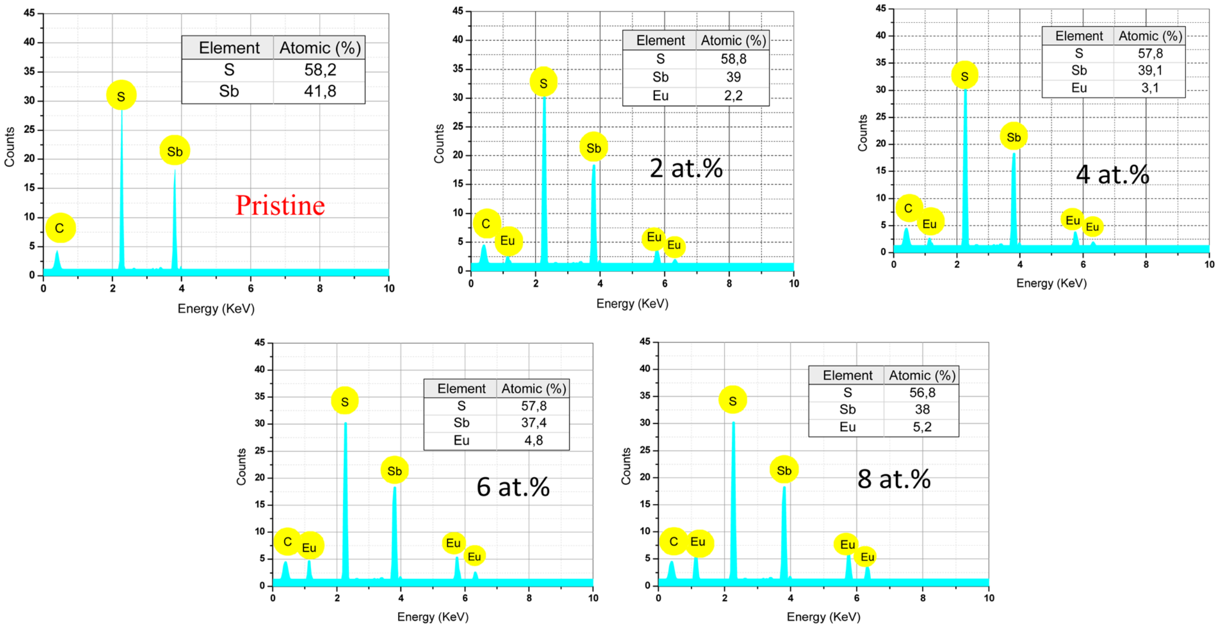

Fig. 7 EDS spectra of Sb_2S_3 thin films, thermally annealed at 300 °C for 5 minutes and doped with varying Eu content, illustrating the elemental composition and the influence of Eu doping on the material's chemical structure.

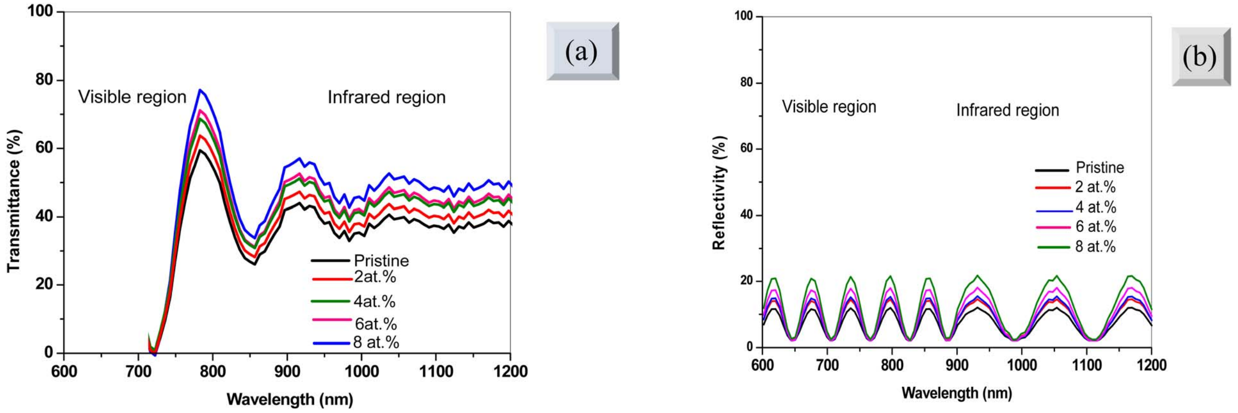

Fig. 8 (a) Spectra of the transmission (*T*) and (b) reflectivity (*R*) for pristine and Eu-doped Sb_2S_3 films at various doping levels, showing the impact of doping on the optical properties of the films.

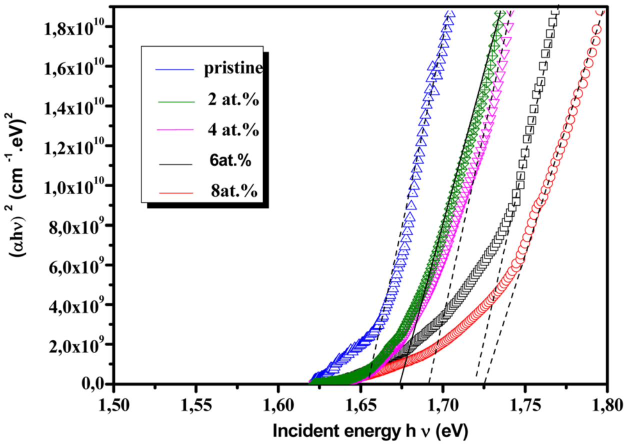

Fig. 9 The optical bandgap of pristine and Eu-doped Sb_2S_3 at various doping levels were analyzed using a Tauc plot derived from the optical transmittance and reflectivity spectra of the glass/Sb_2S_3 layer stack.

Nova software, the Randles equivalent circuit used to fit the EIS results to all the samples is inserted in Fig. 10(a) and the fitting parameters are summarised in Table 3. The obtained resistance values agree with several works published in the literature, where stated resistances for Sb_2S_3 films range between 30 and 700 Ω cm^{-2}.[43] However, the discrepancy between the obtained values and those reported in the literature can be ascribed to different factors such as surface roughness, deposition technique, and the type of substrate used. The high-frequency region typically represents the ohmic resistances (R_s) combinations of the substrate material's and electrolyte's resistances. In contrast, the low-frequency region is dominated by the R_{ct}. The electrode doped with 4 at% Eu^{3+} exhibits the lowest arc radius compared with other samples. This suggests the efficient dynamics of carrier charge separation of photogenerated e^-/h^+ pairs, reduced interfacial charge transfer resistance, and a faster interfacial charge transfer. This result underscores the significance of optimizing Eu doping on the electrical band structure and surface properties of Eu-doped Sb_2S_3 photocatalysts. Thus, the presence of Eu^{3+} ions can improve the charge separation efficiency at the Sb_2S_3/Na_2SO_4 interface and advance the photocatalytic activity.

The photocatalysts were further described for their charge transient processes from Bode plot analysis, as revealed in

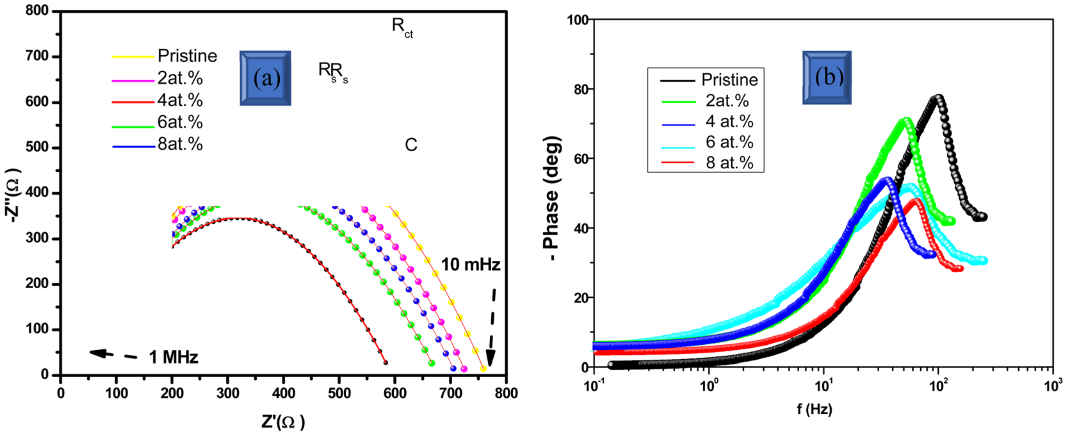

Fig. 10 (a) Electrochemical impedance spectra of pristine and Eu-doped Sb_2S_3. Solid and dashed lines represent the experimental and fitted data, respectively. Inset (a) shows the representation of the Randles equivalent circuit model. (b) Bode phase angle plots for all samples.

Table 3 Fitting of electrical parameters using the Randles equivalent circuit model

Sample	R_s (Ω)	R_{ct} (Ω)	C (Randles) (μF)	C ($\tau = R_{CT} \times C$) (μF)
Pristine	47	760	0.20	0.20
2 at% Eu	48	730	0.50	0.49
4 at% Eu	48	595	1.92	1.80
6 at% Eu	49	710	1.21	1.15
8 at% Eu	49	685	1.00	0.92

Fig. 10(b). The frequency of phase maxima (f_{max}) was established for different photocatalysts, corresponding to the relaxation frequency of photoinduced charge. The lifespan of the electrochemical process was estimated using the peak of the curve in the spectrum, following the mathematical expression:[44]

$$\tau = 1/2\pi f_{\max} \tag{9}$$

where f_{max} is the frequency at the maximum phase angle. The outcomes display that the increase in the Eu doping level prolongs the lifespan of photoinduced electrons. In particular, the sample doped with 4 at% Eu significantly enhances charge separation. The lifespan of photoinduced electrons for 4 at% Eu^{3+} samples is approximately 10 fold higher than that of the pristine sample. The increased lifespan for doped samples indicates the minimum carrier recombination or faster electrochemical process upon Eu doping, due to their morphological variation triggering superior photocatalytic activity. Therefore, the longer lifespan of the photoinduced electrons in the case of 4 at% Eu^{3+}, compared to the pristine sample, is a substantial factor contributing to the enhanced photocatalytic activity.

The electron lifespan, along with the R_{ct} and charge values, can be further used to calculate the capacitance from the Nyquist plot using the electron lifespan $\tau = R_{CT} \times C$.[45] The estimated capacitance of all the samples aligns with the value obtained from the Randle equivalent circuit model. On the other hand, the observed capacitance improvement with the increase of the Eu doping level denotes a significant enhancement in the electron density and effective surface area. These results show an improvement in the surface, as well as an improvement in the bulk properties of the electrode, upon the Eu doping of Sb_2S_3. The decrease in R_{ct}, increase in chemical capacitance, and reduction in electron recombination rate all contribute to the higher photocatalytic activity observed with 4 at% Eu^{3+} doping.

2.6 Hall effect measurements

Hall measurements were conducted to verify charge separation in the Eu-doped Sb_2S_3 photocatalysts, providing valuable insights into the material's electrical transport properties, such as carrier concentration (n or p), Hall mobility (μ_H), resistivity (ρ), Hall coefficient (R_H), and the semiconductor type (n-type or p-type). These parameters are essential for understanding and optimising the material's electrical performance. The conduction mechanism is primarily governed by holes, as proved by the consistently positive R_H (*ca.* 10^{-2} cm^3 C^{-1}) observed across the pristine Sb_2S_3 film. The p-type electrical conductivity is attributed to intrinsic defects, including antisites (S_{Sb}) and sulfur vacancies, which create acceptor levels that facilitate hole conduction, consistent with earlier reports.[46,47] With Eu doping, the Hall coefficient of the Sb_2S_3 film switches from positive to negative as doping levels increase from 0 at% to 8 at%, indicating a change in the majority carrier from holes to electrons. This switching could be due to the impact of metastable hole traps in Sb_2S_3 thin films. Similar p–n switching after doping has been observed in other studies.[48,49] As shown in Table 4, significant changes in resistivity, carrier concentration, and Hall carrier mobility were observed during the Hall measurements. This variation of Hall parameters could be attributed to the decrease in grain size of the Sb_2S_3 thin films as expected by the GIXRD and SEM measurements. The optimal results are obtained at a doping level of 4 at% Eu^{3+}, resulting in a resistivity of 2.5×10^5 Ω cm, and a Hall mobility of 10.25 cm^2 V^{-1} s^{-1}, and an electron density of 3.15×10^{12} cm^{-3}. The analysed Hall coefficient and other Hall parameters suggest that the conduction properties of Sb_2S_3 films can be adjusted through Eu doping. By tuning the amount of Eu doping, it is possible to get lower resistivity and higher charge carrier density. In photocatalysis, lower resistivity (higher mobility) enables photogenerated electrons and holes to move more rapidly within the material, which drops the likelihood of recombination.

2.7 Photocatalytic activity

2.7.1 Photocatalytic degradation of RhB.

Fig. 11 depicts the degradation rate of RhB dye by all Sb_2S_3 thin films under dark conditions, visible light (a cut-off filter $\lambda > 420$ nm), simulated sunlight (without the 420 nm cutoff filter), and UV light irradiation (a band-pass filter $\lambda < 380$ nm). Under visible light irradiation, about 80% of RhB dye degradation was attained after 120 min of photocatalytic reaction, while under UV light irradiation the attained degradation percentage drops to

Table 4 Experimental results of conductivity type, Hall mobility, resistivity, and carrier concentration measured at room temperature for different Eu doping levels

Sample	Conductivity	μ_H (cm^2 V^{-1} s^{-1})	ρ (kΩ cm)	Carrier density (cm^{-3})
Pristine Sb_2S_3	p	9.85	2.9×10^2	2.87×10^{12}
2 at% Eu	n	10.12	2.7×10^2	3.05×10^{12}
4 at% Eu	n	10.25	2.5×10^2	3.15×10^{12}
6 at% Eu	n	9.56	3.1×10^2	2.95×10^{12}
8 at% Eu	n	9.45	3.4×10^2	2.05×10^{12}

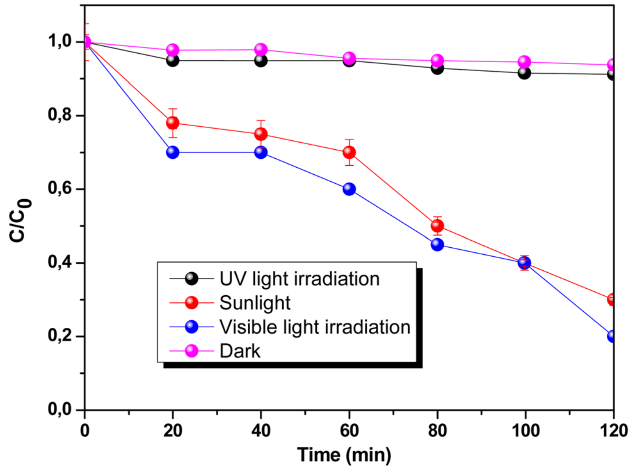

Fig. 11 Plot of C/C_0 *versus* time *via* the pristine Sb_2S_3 and Eu-doped Sb_2S_3 films at various doping levels within 120 min at room temperature and atmospheric pressure, under dark conditions and light irradiations.

approximately 3% within 120 min. This is because all the Sb_2S_3 samples have their highest absorbance peak at the visible range, not in the UV spectra. In other words, all the Sb_2S_3 samples were impotent for degraded RhB under UV light irradiation as well as dark conditions. Since the highest degree of dye removal was recorded under visible light irradiation. Therefore, our emphasis shifted to the photocatalytic activity of the synthesized samples under visible light only, which would provide valuable insights for future applications. The processes of RhB removal on Eu-doped Sb_2S_3 photocatalysts at different doping levels under dark and visible light irradiation are shown in Fig. 12(a and b). It can be seen that the removal of RhB dye by all Sb_2S_3 photocatalysts under visible light irradiation is about three times greater than in the dark after 120 minutes. The removal of RhB dye under dark conditions could be ascribed to the catalytic surface properties of Sb_2S_3.[50] On the other hand, Eu^{3+} ions significantly impacted the photocatalytic activity of Sb_2S_3 photocatalysts, as shown in Fig. 12(b). The pristine film removed *ca.* 39.1% of the RhB within 120 min. However, the Eu-doped Sb_2S_3 photocatalyst exhibited significant photocatalytic activity, especially at the Eu doping level of 4 at%, where *ca.* 90.99% of RhB was removed with the highest photocatalytic rate. This behaviour might be attributed to the large surface area, which usually has more active sites to absorb organic molecules.[51] As the dopant level increases, the particle size decreases, leading to an increase in surface area and a reduction in degradation efficiency. In addition, RhB showed minimal photodegradation under visible light irradiation.[52] Therefore, the removal of RhB was also attributed to the photocatalytic degradation facilitated by the photocatalyst. Beyond the doping level of 4 at%, the ratio of removed RhB decreased to 89.3% possibly due to the presence of Eu_2O_3 phase and/or the excess of vacancies generated, which act as recombination centres rather than electron scavengers. This finding highlights the potential of Eu-doped Sb_2S_3 as an effective photocatalyst for degrading RhB, since 4 at% Eu-doped Sb_2S_3 showed maximum efficiency, further studies were performed using 4 at% Eu-doped Sb_2S_3. As shown in Fig. 13(a and b), the temporal evolution of the absorbance spectra of RhB dye solution was monitored in dark and visible light conditions at regular time intervals of 20 min in the presence of the Eu-doped Sb_2S_3 photocatalyst with a doping level of 4 at%. The significant decrease in the intensity of the principal absorption peak of the RhB dye suggests that adsorption of the RhB dye is occurring. The gradual decrease in the intensity of the absorbance peak of RhB signifies its decomposition over time in both dark and visible light conditions. It could also be seen that approximately 95% of the simulated RhB wastewater was adsorbed within 120 min in visible light conditions, which is probably attributed to the availability of more active sites. Over time, the colour of the wastewater varied gradually from magenta to colourless, as shown in the inset of Fig. 13(b). On the other hand, no shift in λ_{max} was observed throughout the entire course of the RhB degradation in the presence of Eu-doped Sb_2S_3 photocatalyst. This suggests that the degradation of RhB dye mainly occurs *via* photocatalysis. This outcome underscores the promising

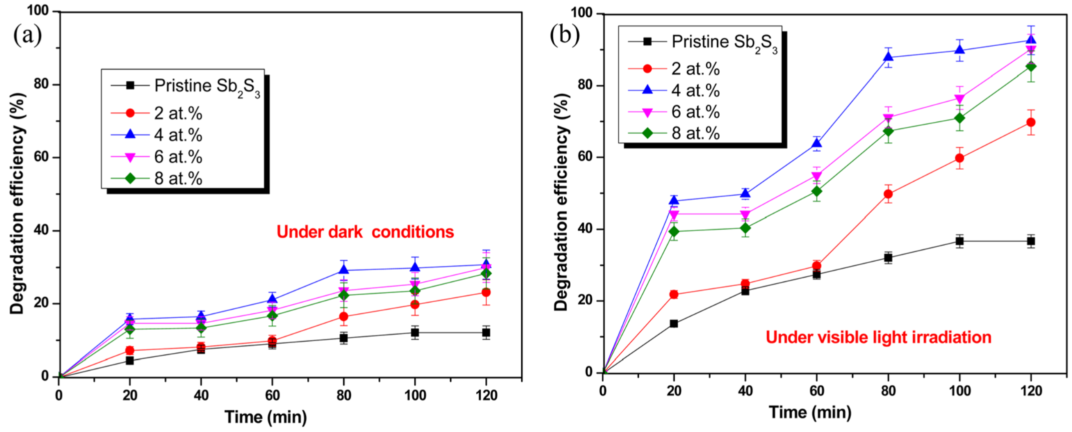

Fig. 12 The photocatalytic degradation efficiency of RhB dye *via* the pristine Sb_2S_3 and Eu-doped Sb_2S_3 photocatalysts at various doping levels within 120 min (a) under dark conditions (b) under visible light irradiation.

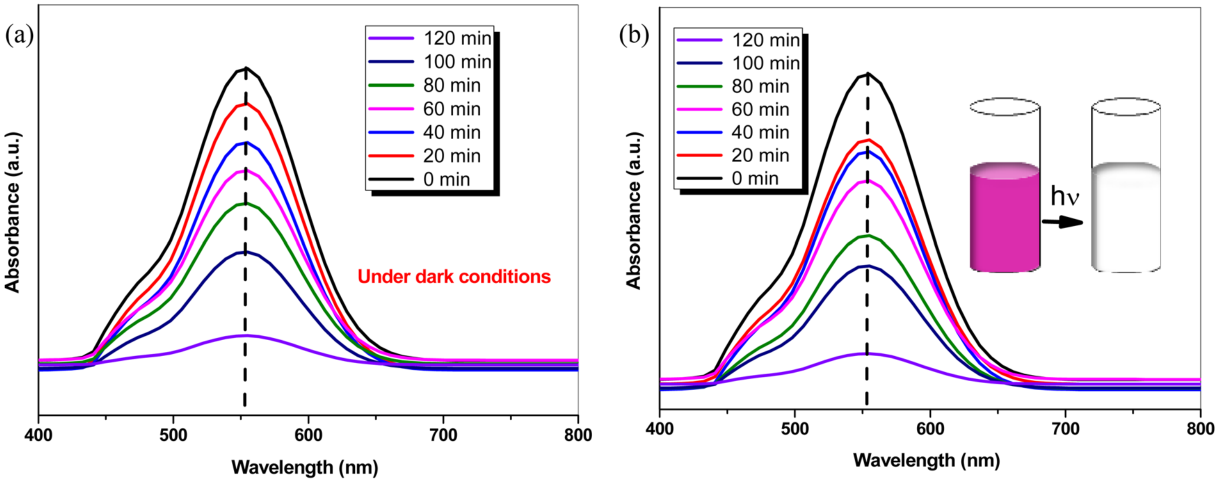

Fig. 13 Temporal evolution of the absorbance spectra of RhB dye solution (a) under dark conditions (b) under visible light irradiation in the presence of 4 at% Eu-doped Sb_2S_3 photocatalyst. The intensity of the absorbance band at 554 nm decreases as the RhB degrades, indicating the photocatalytic activity of the films.

potential of Eu-doped Sb_2S_3 as an effective catalyst in environmental remediation applications.

2.7.2 **Recyclability.** To evaluate the recyclability of the synthesized catalysts, the Eu-doped Sb_2S_3 photocatalyst with 4 at% doping level was selected for recycling experiments. As illustrated in Fig. S1,† after five cycles, the quantity of degraded RhB diminished by approximately 5%, namely from 95.1% to 90% of the initial RhB quantity. While there was a slight decrease in the photocatalytic performance of the catalyst during the degradation process, it remained effective. The decline in RhB removal efficiency could be ascribed to the accumulation of RhB on the photocatalyst surface, which hindered the adsorption of RhB from the solution. Furthermore, the GIXRD pattern of the Eu-doped Sb_2S_3 photocatalyst with a doping level of 4 at% after five cycles of reuse is delineated in Fig. S2.† No significant differences in the diffraction peaks are detected, confirming a highly stable crystal structure. The high stability of this photocatalyst is attributed to the good crystalline structure of Eu-doped Sb_2S_3 that significantly reduced the defects' density and effectively inhibited the photo corrosion of the Sb_2S_3 thin film. Consequently, Sb_2S_3 demonstrates potential as an efficient photocatalyst for applications in wastewater treatment.

2.7.3 **Kinetic study.** Various kinetic models can be applied to the experimental data to achieve a quantitative insight of the RhB degradation reaction kinetics and the characteristic constant associated with RhB degradation by Eu-doped Sb_2S_3 with a doping level of 4 at%. The kinetics of photocatalysis were investigated using Lagergren pseudo-first-order and pseudo-second-order models to fit the experimental data, as expressed below:[53]

$$\frac{dq}{dt} = k_1(q_e - q_t) \tag{10}$$

$$\frac{dq}{dt} = k_2(q_e - q_t)^2 \tag{11}$$

where q_e and q_t (mg g^{-1}) are the amounts remaining after the equilibrium reaction of the RhB dye and the amount adsorbed at time t (min), respectively, k_1 (min^{-1}) and k_2 (g mg^{-1} min^{-1}) are the kinetic rate constant of pseudo-first-order and pseudo-second-order degradation, respectively. Fig. 14(a and b) shows the pseudo-first-order and pseudo-second-order kinetic models of the degradation chemical reaction of RhB dye. The goodness of fit of the reaction order could be determined from the regression correlation coefficient (R^2) of the kinetics plots. The calculated R^2 value for the first-order rate model was roughly higher than the second-order rate model. This outcome suggests that the pseudo-first-order model of RhB's adsorption kinetics on Eu-doped Sb_2S_3 with a doping level of 4 at% provides more in-depth information. This implies that the kinetics could be characterized as physisorption due to van der Waals interactions between the Eu-doped Sb_2S_3 and RhB dye. Other findings also support the pseudo-first-order kinetics for RhB dye adsorption onto photocatalysts. R. Thayil *et al.* demonstrated that the photodegradation process of RhB dyes using MoS_2 photocatalysts, primarily governed by van der Waals interactions, conforms to a pseudo-first-order adsorption kinetic model.[54] The estimated rate constant of pseudo-first-order k_1 was found about 0.049 min^{-1}. This value significantly differs from the kinetic rate obtained with a second-order rate model, which falls below 0.007 g mg^{-1} min^{-1}.

2.7.4 **Scavenger study.** Radical scavenging experiments are a powerful method for elucidating the specific roles of different radicals in the degradation of pollutants. By selectively quenching certain reactive species with appropriate scavengers, researchers can infer the contributions of these radicals to the overall degradation process. This approach helps to unearth the complex mechanisms involved in photocatalytic reactions and provides valuable insights for optimizing photocatalysts for environmental remediation applications. Different scavengers such as IPA, EDTA, K_2CrO_7, and *p*-BQ were added independently to the RhB dye solution to identify the active radicals present

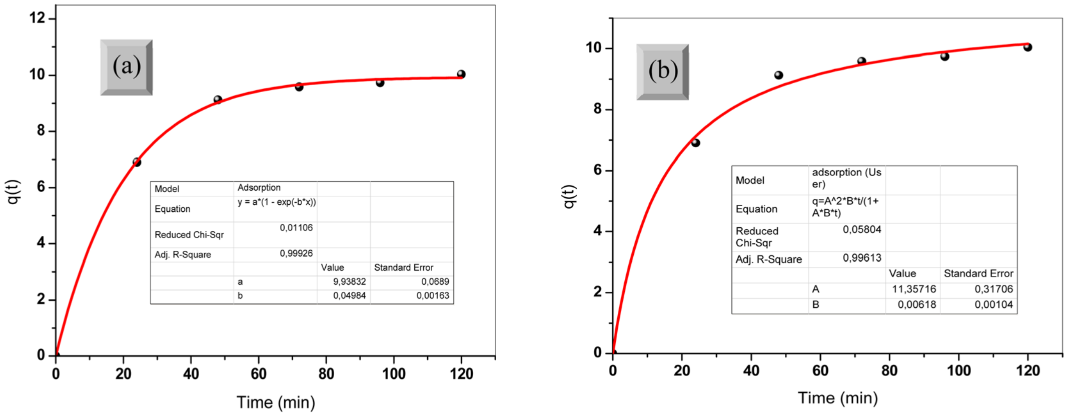

Model	Adsorption		
Equation	y = a*(1 - exp(-b*x))		
Reduced Chi-Sqr	0,01106		
Adj. R-Square	0,99926		
		Value	Standard Error
	a	9,93832	0,0689
	b	0,04984	0,00163

Model	adsorption (User)		
Equation	q=A^2*B*t/(1+A*B*t)		
Reduced Chi-Sqr	0,05804		
Adj. R-Square	0,99613		
		Value	Standard Error
	A	11,35716	0,31706
	B	0,00618	0,00104

Fig. 14 The adsorption kinetic plots of RhB on 4 at% Eu-doped Sb_2S_3 film fitted with (a) pseudo-first-order, and (b) pseudo-second-order models.

during the photocatalysis experiment. These scavengers selectively capture specific active radicals, allowing us to discern their contributions to the photocatalytic degradation process. IPA is commonly used as a scavenger for $^{\bullet}OH$ radicals,[55] EDTA as a scavenger for h^+,[56] K_2CrO_7 as a scavenger for e^-,[57] and *p*-BQ as a scavenger for $^{\bullet}O_2^-$.[58] Fig. 15 delineates the effect of scavenging radicals on the dye degradation efficiency of the Eu-doped Sb_2S_3 (4 at%) photocatalysts for RhB dye. The results indicated that RhB dye can be completely degraded without a scavenger. However, when *p*-BQ was added to the reaction solution, RhB degradation was irrelevantly inhibited, and about 20% of RhB was degraded after 120 min of light irradiation. Another inhibition phenomenon for the photocatalytic reaction appeared in the presence of IPA. Indeed, when IPA was added to the reaction solution, the degradation efficiency of RhB over the Eu-doped Sb_2S_3 (4 at%) decreased, resulting in only 40% of RhB degradation after 120 min of light irradiation. Nevertheless, the addition of K_2CrO_7 and EDTA scavengers did not significantly change the photocatalytic degradation of RhB compared with the absence of scavengers. In the process of RhB degradation, $^{\bullet}O_2^-$ and $^{\bullet}OH$ are identified as the principal oxidative species, in contrast to e^- and h^+, which play a less significant role.

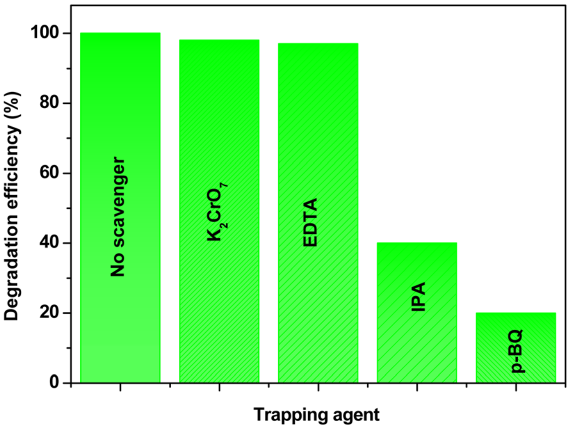

Fig. 15 Radical scavenger study for active species during the photodegradation of RhB wastewater employing Eu-doped Sb_2S_3 (4 at%) photocatalyst under visible light.

2.7.5 Photocatalytic mechanism. The expected photocatalytic mechanism of the Eu-doped Sb_2S_3 (4 at%) toward RhB dye is exhibited in Fig. 16. When visible light irradiates the Eu-doped Sb_2S_3 semiconductor photocatalyst, e^-/h^+ pairs are generated. The generated e^-/h^+ pairs are involved in the decomposition and oxidation processes of the RhB dye in the aqueous solution. Indeed, these generated pairs migrate to the surface of the Eu-doped Sb_2S_3 photocatalyst, where they can react with the RhB dye. The h^+ in the valence band (VB) migrates towards the surface and reacts with water molecules (H_2O), generating ($^{\bullet}OH$) radicals, which are effective oxidizing species responsible for decomposing RhB dye.[59] This process ultimately boosts the photocatalytic degradation efficiency. Meanwhile, the e^- in the conduction band (CB) reacted with hydrogen peroxide (H_2O_2) and Eu^{3+} ions on the catalyst's surface to produce $^{\bullet}OH$ radicals. On one side, the e^- in the CB reacts with dissolved oxygen (O_2) to yield superoxide ions ($^{\bullet}O_2^-$), which inhibits e^-/h^+ pairs recombination.[60] This reaction stabilizes the charge carriers and generates reactive oxygen species (ROS) that are crucial for the degradation of organic pollutants in photocatalytic processes. As we know, $^{\bullet}O_2^-$ radicals are less reactive than $^{\bullet}OH$ and hydroperoxy ($^{\bullet}O_2H$) ones.[61] Thus, it cannot react with most molecules in an aqueous solution. However, $^{\bullet}O_2H$ radicals decomposed into H_2O_2, which combined with $^{\bullet}O_2^-$ radicals to yield $^{\bullet}OH$ radicals. On the other hand, the Eu^{3+} ions act as scavengers for e^- in the CB, preventing the recombination of e^-/h^+ pairs. This process is possible since the Eu^{3+} ions are stable owing to their half-filled orbitals ([Xe]$4f^6$).[62,63] Nevertheless, this stability is disrupted when the Eu^{3+} ions trap e^- from the CB to produce Eu^{2+}. The Eu^{2+} ions formed attempt to return to a stable Eu^{3+} state by transferring an e^- to an oxygen molecule (O_2), which conducts the formation of a superoxide ion (O_2^-), contributing towards RhB degradation. The pathways of photocatalytic reactions are described by the following equations:

$$Sb_2S_3 + h\nu \rightarrow e^- + h^+ \tag{12}$$

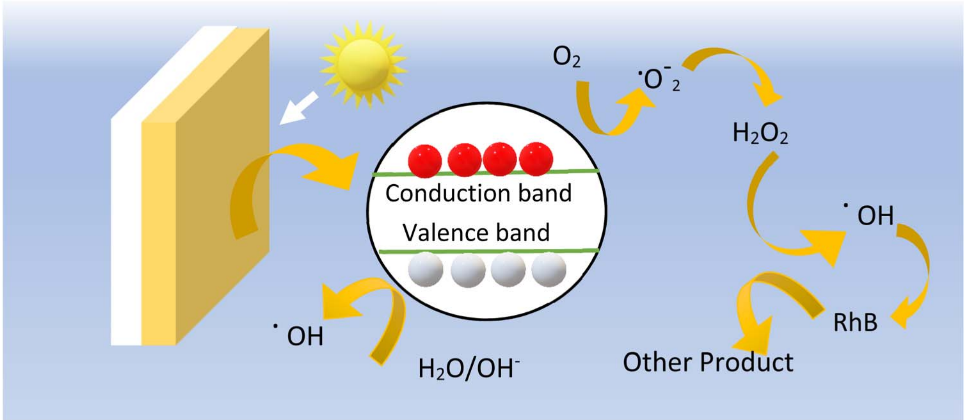

Fig. 16 The mechanism of the Eu-doped Sb_2S_3 (4 at%) photocatalyst activity toward RhB dye under visible light irradiation.

$$h^+ + H_2O \rightarrow {}^{\bullet}OH + H^+ \quad (13)$$

$$e^- + O_2 \rightarrow {}^{\bullet}O_2^- \quad (14)$$

$${}^{\bullet}O_2^- + H^+ \rightarrow {}^{\bullet}HO_2 \quad (15)$$

$$2{}^{\bullet}HO_2 \rightarrow O_2 + H_2O_2 \quad (16)$$

$$H_2O_2 + {}^{\bullet}O_2– \rightarrow OH^- + {}^{\bullet}OH + O_2 \quad (17)$$

$$Eu^{3+} + e^- \rightarrow Eu^{2+} \quad (18)$$

$$Eu^{2+} + O_2 \rightarrow Eu^{3+} + O_2^- \quad (19)$$

$$Eu^{3+} + {}^{\bullet}HO^- + h^+ \rightarrow Eu^{3+} + {}^{\bullet}OHx \quad (20)$$

$$\text{Dye (RhB)} + {}^{\bullet}OH \rightarrow \text{degradation products} \quad (21)$$

These outcomes show that $^{\bullet}O_2^-$ is the significant active species for the degradation of RhB by Eu-doped Sb_2S_3 (4 at%) photocatalyst under visible light irradiation, while $^{\bullet}OH$ acted a supplementary role throughout the photocatalytic process. Zhang *et al.* found that O_2^- and $^{\bullet}OH$ radicals were the main oxidative species during the degradation of methyl orange (MO) dye under visible light irradiation in the presence of Sb_2S_3 nanowires photocatalysts.[64] Moreover, they believed that the photocatalytic activity can be boosted by the larger specific surface area of catalysts because of the less steric hindrance for the diffusion of reactants. This underscores the importance of examining the photocatalytic mechanism for each specific dye/catalyst pair under chosen conditions.

3. Conclusion

In this study, Eu-doped Sb_2S_3 photocatalysts were synthesized using a simple and cost-effective dip-coating technique to enhance their efficiency for photocatalytic applications. The synthesized photocatalysts were characterized using microscopic and spectroscopic techniques to investigate their structural, morphological, and optical properties. GIXRD, SEM, EDX, and Raman spectroscopy analyses corroborated the single-phase orthorhombic crystal structure of Sb_2S_3 and the effective incorporation of the europium element. GIXRD measurements reveal an average crystallite size ranging from 35 to 18 nm as the Eu doping level increases. By the way, the Raman data showed a higher Eu content (>4 at%) could induce lattice distortion and weaken the film's crystallinity, leading to increased segregation of Eu^{3+} ions in the grain GBs. The optical band gap increases from 1.67 to 1.72 eV as the doping level increases from 0 to 8 at%, suggesting band edge bending. The EIS measurement revealed the lowest R_{ct} at 4 at% of Eu doping, indicating efficient electron transport and a reduced recombination rate of photogenerated charge carriers. The visible-light-driven photodegradation rate for simulated wastewater containing RhB organic dye was achieved at the optimal doping level of 4 at% Eu, representing approximately 98.2% degradation. Lastly, the dye degradation mechanism was deduced based on the scavenger studies.

Data availability

The data supporting this article have been included as part of the ESI.†

Conflicts of interest

The author confirms that there are no known competing financial interests or personal relationships associated with this publication for this work that could have influenced its outcome.

Acknowledgements

I enthusiastically acknowledge financial support from the Center of Research and Technology of Energy, Technopole of Borj Cedria, Tunisia.

References

1 A. Rahman and M. M. Khan, Chalcogenides as photocatalysts, *New J. Chem.*, 2021, **45**, 19622–19635.

2 M. S. Siddiqui and M. Aslam, *Chalcogenides as Well as Chalcogenides-Based Nanomaterials and its Importance in Photocatalysis, Chalcogenide-Based Nanomaterials as Photocatalysts*, Elsevier, Amsterdam, 2021, pp. 33–76.

3 X.-L. Zheng, Y.-J. Yang, Y.-H. Liu, P.-L. Deng, J. Li, W.-F. Liu, P. Rao, C.-M. Jia, W. Huang, Y.-L. Du, Y.-J. Shen and X.-L. Tian, Fundamentals and photocatalytic hydrogen evolution applications of quaternary chalcogenide semiconductor: Cu_2ZnSnS_4, *Rare Met.*, 2022, **41**, 2153–2168.

4 M. D. Regulacio and M.-Y. Han, Multinary I-III-VI_2 and I_2-II-IV-VI_4 Semiconductor Nanostructures for Photocatalytic Applications, *Acc. Chem. Res.*, 2016, **49**(3), 511–519.

5 M. M. Khan, *Chalcogenide-Based Nanomaterials as Photocatalysts*, ed. M. M. Khan, Elsevier, 1st edn, 2021.

6 J. A. Christians, D. T. Leighton Jr and P. V. Kamat, Rate limiting interfacial hole transfer in Sb_2S_3 solid-state solar cells, *Energy Environ. Sci.*, 2014, **7**, 1148–1158.

7 W. Zhang, M. Tan, P. Zhang, L. N. Zhang, W. N. Dong, Q. S. Wang, J. W. Ma, E. L. Dong, S. C. Xu and G. Q. Wang, one-pot synthesis of Sb_2S_3 nanocrystalline films through a PVP-assisted hydrothermal process, *Appl. Surf. Sci.*, 2018, **455**, 1063–1069.

8 R. Nie, K. S. Lee, M. Hu and S. I. Seok, Strain Tuning via Larger Cation and Anion Codoping for Efficient and Stable Antimony-Based Solar Cells, *Adv. Sci.*, 2021, **8**(1), 2002391.

9 S. A. Zaki, M. I. Abd-Elrahman and A. A. Abu-Sehly, Optical and electrical properties of amorphous Sb_2S_3 thin films: Effect of the film thickness, *J. Non-Cryst. Solids*, 2021, **552**, 120318.

10 V. Rotaru, P. Vidal-Fuentes, X. Alcobe, T. Jawhari, A. López-García, A. Pérez-Rodríguez, I. Becerril-Romero, V. Izquierdo-Roca and M. Guc, Structural and vibrational properties of Sb_2S_3: Practical methodologies for accelerated research and application of this low dimensional material, *iScience*, 2024, **27**(4), 109619.

11 M. A. Farhana, A. Manjceevan and J. Bandara, Recent advances and new research trends in Sb_2S_3 thin film based solar cells, *J. Sci.: Adv. Mater. Devices*, 2023, **8**, 100533.

12 Z. Cai, C. M. Dai and S. Chen, Intrinsic Defect Limit to the Electrical Conductivity and a Two-Stepp-Type Doping Strategy for Overcoming the Efficiency Bottleneck of Sb_2S_3-Based Solar Cells, *Sol. RRL*, 2020, **4**, 1900503.

13 J. Lin, A. Mahmood, G. Chen, N. Ahmad, M. Chen, P. Fan, S. Chen, R. Tang and G. Liang, Crystallographic orientation control and defect passivation for high efficient antimony selenide thin-film solar cells, *Mater. Today Phys.*, 2022, **27**, 100772.

14 I. L. P. Raj, A. J. Christy, R. David Prabu, N. Chidhambaram, M. Shkir, S. AlFaify and A. Khan, Significance of Ni doping on structure-morphology-photoluminescence, optical and photocatalytic activity of CBD grown ZnO nanowires for opto-photocatalyst applications, *Inorg. Chem. Commun.*, 2020, **119**, 108082.

15 Z. Wang, L. Li, L. Hong, X. Shi, Y. Lu and J. Su, Bi-doped Sb_2S_3 Thin Film Synthesized by a Two-Step Approach with Enhanced Photoelectrochemical Water Splitting Performance, *J. Electrochem. Soc.*, 2022, **169**, 066508.

16 A. Chihi, Effect of Ruthenium doping in tailoring structure, optical and electrical properties of Sb_2S_3 thin film synthesized via electrodeposition technique, *J. Mater. Sci.: Mater. Electron.*, 2023, **34**, 2087.

17 T. Stamenkovi, N. Bundaleski, T. Barudzija, I. Validzi and V. Lojpur, XPS study of iodine and tin-doped Sb_2S_3 nanostructures affected by non-uniform charging, *Appl. Surf. Sci.*, 2021, **567**, 150822.

18 T. Aitasalo, P. Dereń, J. Hölsä, H. Jungner, J.-C. Krupa, M. Lastusaari, J. Legendziewicz, J. Niittykoski and W. Stręk, Persistent luminescence phenomena in materials doped with rare earth ions, *J. Solid State Chem.*, 2003, **171**, 114–122.

19 X. Liu, L. Zhang, W. Jin, Q. Li, Q. Sun, Y. Wang, E. Liu, X. Hu and H. Miao, Epitaxial growth strategy for construction of Tm^{3+} doped and [hk1] oriented Sb_2S_3 nanorods S-scheme heterojunction with enhanced photoelectrochemical performance, *Chem. Eng. J.*, 2023, **475**(1), 146315.

20 T. Zhang, Z. Wang, H. Xiang, X. Xu, J. Zou and C. Lu, Biocompatible Superparamagnetic Europium-Doped Iron Oxide Nanoparticle Clusters as Multifunctional Nanoprobes for Multimodal In Vivo Imaging, *ACS Appl. Mater. Interfaces*, 2021, **13**(29), 33850–33861.

21 R. Kondrotas, C. Chen and J. Tang, Sb_2S_3 solar cells, *Joule*, 2018, **2**, 857–878.

22 N. Miniajluk-Gaweł, R. Tomala, B. Bondzior, B. Bondzior and P. J. Dereń, Influence of Sintering Parameters on Spectroscopic Properties of BMW: Eu^{3+} Ceramic Materials Prepared by HPLT Technique, *Materials*, 2022, **15**(21), 7410.

23 W. Ran, H. M. Noh, S. H. Park, B. K. Moon, J. H. Jeong, J. H. Kim and J. Shi, Break the Interacting Bridge between Eu^{3+} Ions in the 3D Network Structure of $CdMoO_4$:Eu^{3+} Bright Red Emission Phosphor, *Sci. Rep.*, 2018, **8**, 5936.

24 U. Wahl, J. G. Correia, S. Decoster and T. Mendonca, Lattice location of the group V elements As and Sb in ZnO, *Phys. B*, 2009, **404**, 4803–4806.

25 V. D. Mote, Y. Purushotham and B. N. Dole, Williamson-Hall analysis in estimation of lattice strain in nanometer-sized ZnO particles, *J. Theor. Appl. Phys.*, 2012, **6**, 6.

26 T. Jiang, Y. Wang, D. Meng and D. Wang, One-step hydrothermal synthesis and enhanced photocatalytic performance of pine-needle-like Zn-doped CuO nanostructures, *J. Mater. Sci.: Mater. Electron.*, 2016, **27**, 12884–12890.

27 A. Chihi, Impact of Ag-coating on CAS thin film for boosted photoelectrochemical water splitting, *Appl. Phys. A*, 2023, **129**, 472.

28 A. Chihi and B. Bessais, Correlation Between Microstructure and Optical Properties of Cu ($In_{0.7}$, $Ga_{0.3}$) Se_2 Grown by Electrodeposition Technique, *J. Electron. Mater.*, 2017, **46**, 354–362.

29 Y. Liu, K. T. E. Chua, T. C. Sum and C. K. Gan, First-principles study of the lattice dynamics of Sb_2S_3, *Phys. Chem. Chem. Phys.*, 2014, **16**, 345.

30 V. Rotaru, P. Vidal-Fuentes, X. Alcobe, T. Jawhari, A. López-García, A. Pérez-Rodríguez, I. Becerril-Romero, V. Izquierdo-Roca and M. Guc, Structural and vibrational

properties of Sb_2S_3: Practical methodologies for accelerated research and application of this low dimensional material, *iScience*, 2024, **27**, 109619.

31 M. Delaney, I. Zemeckis, D. Lawson, D. W. Hewak and O. L. Muskens, A New Family of Ultralow Loss Reversible Phase-Change Materials for Photonic Integrated Circuits: Sb_2S_3 and Sb_2Se_3, *Adv. Funct. Mater.*, 2020, **30**, 1–10.

32 J. S. Eensalu, K. Tõnsuaadu, I. O. Acik and M. Krunks, Sb_2S_3 thin films by ultrasonic spray pyrolysis of antimony ethyl xanthate, *Mater. Sci. Semicond. Process.*, 2022, **137**, 106209.

33 S. M. Hwang, J. Kim, Y. Kim and Y. Kim, Na-ion storage performance of amorphous Sb_2S_3 nanoparticles: anode for Na-ion batteries and seawater flow batteries, *J. Mater. Chem. A*, 2016, **4**, 17946–17951.

34 A. Chihi, Annealing effect on Sb_2S_3/c-Si structure for photovoltaic applications, *Appl. Phys. A*, 2024, **130**, 532.

35 J.-G. Kang, Y. Jung, B.-K. Min and Y. Sohn, Full characterization of $Eu(OH)_3$ and Eu_2O_3 nanorods, *Appl. Surf. Sci.*, 2014, **314**, 158–165.

36 M. Myilsamy, M. Mahalakshmi, N. Subha, A. Rajabhuvaneswari and V. Murugesan, Visible light responsive mesoporous graphene-Eu_2O_3/TiO_2 nanocomposites for the efficient photocatalytic degradation of 4-chlorophenol, *RSC Adv.*, 2016, **6**(41), 35024–35035.

37 R. Basumatary, S. Sahu, D. Goyari, D. Pamu and R. Brahma, Effect of manganese (Mn) doping on the structural, dielectric, ferroelectric, and ferromagnetic properties of ceria (CeO_2), *J. Alloys Compd.*, 2024, **999**, 174958.

38 R. Murugan, G. Vijayaprasath, M. Thangaraj, T. Mahalingam, S. Rajendran, M. Arivanandhan, A. Loganathan, Y. Hayakawa and G. Ravi, Defect assisted room temperature ferromagnetism on rf sputtered Mn doped CeO_2 thin films, *Ceram. Int.*, 2017, **43**(1), 399–406.

39 M. Zhang, T. Caldwell, A. L. Hector, N. Garcia-Araez and J. Falvey, Solvothermal synthesis of nanoscale $BaTiO_3$ in benzyl alcohol-water mixtures and effects of manganese oxide coating to enhance the PTCR effect, *Dalton Trans.*, 2023, **52**, 297–307.

40 S. Salinas-Beltrán, J. R. Gaitán-Arevalo and L. A. González, Improvement of the photoelectrical properties of chemical bath-deposited Sb_2S_3 thin films with low copper doping, *J. Mater. Sci.: Mater. Electron.*, 2024, **35**, 458.

41 U. Chalapathi, B. Poornaprakash and S. H. Park, The effect of Cu-doping on the structural, microstructural, optical, and electrical properties of Sb_2S_3 thin films, *Chalcogenide Lett.*, 2019, **16**, 449.

42 A. A. M. Faraga, M. I. Mohammed, V. Ganesh, H. Elhosiny Ali, A. M. Aboraiae, Y. Khairy, H. H. Hegazy, V. Butova, A. V. Soldatov, H. Algarni, H. Y. Zahran and I. S. Yahia, Investigating the influence of Eu-doping on the structural and optical characterisation of cadmium oxide thin films, *Optik*, 2023, **281**, 170830.

43 Z. Wang, L. Li, L. Hong, X. Shi, Y. Lu and J. Su, Bi-Doped Sb_2S_3 Thin Film Synthesized by a Two-Step Approach with Enhanced Photoelectrochemical Water Splitting Performance, *J. Electrochem. Soc.*, 2022, **169**, 066508.

44 S. Nayak and K. Parida, Superlative photoelectrochemical properties of 3D MgCr-LDH nanoparticles influencing towards photoinduced water splitting reactions, *Sci. Rep.*, 2022, **12**, 9264.

45 H. K. Zafar, M. Sohail, A. Nafady, K. K. Ostrikov, G. Will, Md A. Wahab and A. P. O'Mullane, S-doped copper selenide thin films synthesized by chemical bath deposition for photoelectrochemical water splitting, *Appl. Surf. Sci.*, 2023, **641**, 158505.

46 L. Guo, B. Zhang, S. Li, Q. Zhang, M. Buettner, L. Li, X. Qian and F. Yan, Scalable and efficient Sb_2S_3 thin-film solar cells fabricated by close space sublimation, *APL Mater.*, 2019, **7**, 041105.

47 Z. Ma, Y. Yang, X. Wei, Q. Li, D. Zhang, Y. Wang, Y. Wang, E. Liu and H. Miao, CdSe Quantum Dots Supported on Sb_2S_3 Nanorods as S-Scheme Heterojunction Photoanode in Photoelectrochemical Cells, *ACS Appl. Nano Mater.*, 2024, **7**(20), 24213–24223.

48 J. Ivkov, N. Radić and A. Tonejc, Hall effect in Al-W thin films, *Solid State Commun.*, 2004, **129**(6), 369–373.

49 F. B. Mebid and A. A. A. Shihab, Effect of aluminium impurities on some properties of amorphous As_2Se_3 thin films, *AIP Conf. Proc.*, 2023, **2475**, 090024.

50 E. Aslan, G. Sahin and A. Goktas, Facile synthesis of Sb_2S_3 micro-materials for highly sensitive visible light photodetectors and photocatalytic applications, *Mater. Chem. Phys.*, 2023, **307**, 128160.

51 N. D. Raskar, D. V. Dake, V. A. Mane, E. Stathatos, U. Deshpande and B. Dole, One-step synthesis of vertically grown Mn-doped ZnO nanorods for photocatalytic application, *J. Mater. Sci.: Mater. Electron.*, 2019, **30**, 10886–10899.

52 X. Wang, X. Wang, J. Zhao, J. Chen, J. Zhang, J. Song and J. Huang, Bioframe synthesis of NF–TiO_2/straw charcoal composites for enhanced adsorption-visible light photocatalytic degradation of RhB, *RSC Adv.*, 2015, **5**, 66611–66620.

53 G. Zhu, Q. Liu, F. Cao, Q. Qin and M. Jiao, Silkworm cocoon derived N, O-codoped hierarchical porous carbon with ultrahigh specific surface area for efficient capture of methylene blue with exceptionally high uptake: kinetics, isotherm, and thermodynamics, *RSC Adv.*, 2019, **9**, 33872–33882.

54 R. Thayil and S. Cherukulappurath, SERS-based detection of efficient removal of organic dyes using molybdenum dichalcogenide nanostructures, *Nano Express*, 2023, **4**(3), 035005.

55 Y. Ke, H. Guo, D. Wang, J. Chen and W. Weng, ZrO_2/g-C_3N_4 with enhanced photocatalytic degradation of methylene blue under visible light irradiation, *J. Mater. Res.*, 2014, **29**(20), 2473–2482.

56 N. K. Gupta, Y. Ghaffari, S. Kim, J. Bae, K. S. Kim and M. Saifuddin, Photocatalytic Degradation of Organic Pollutants over MFe_2O_4 (M = Co, Ni, Cu, Zn) Nanoparticles at Neutral pH, *Sci. Rep.*, 2020, **10**, 4942.

57 J. A. Christians, D. T. Leighton Jr and P. V. Kamat, Rate limiting interfacial hole transfer in Sb_2S_3 solid-state solar cells, *Energy Environ. Sci.*, 2014, **7**, 1148–1158.

58 A. Chihi, Hydrothermal synthesis of chalcostibite nanoflowers with enhanced visible light photocatalytic activity, *Optik*, 2022, **271**, 170142.

59 Y. Chen, H. Liu, B. Geng, J. Ru, C. Cheng, Y. Zhao and L. Wang, A reusable surface-quaternized nano cellulose-based hybrid cryogel loaded with N-doped TiO_2 for self-integrated adsorption/photo-degradation of methyl orange dye, *RSC Adv.*, 2017, **7**, 17279–17288.

60 U. R. Bagwan, I. N. Shaikh, R. S. Malladi, A. L. Harihar and S. M. Hunagund, Effect of TiO_2 and Gadolinium dopants on photocatalytic behavior for Acriflavine dye, *J. Rare Earths*, 2020, **38**(3), 234–240.

61 D. J. Charles, Cardamom, *Antioxidant Properties of Spices, Herbs, and Other Sources*, 2012, pp. 207–212.

62 J.-C. Bünzli, Europium in the limelight, *Nat. Chem.*, 2010, **2**, 696.

63 A. Patej, J. Hanuza, M. Ptak, A. Pelczarska, I. Szczygiel, R. J. Wiglusz and A. Watras, Influence of synthesis conditions on structural and spectroscopic properties of the $K_2SrP_2O_7$ pyrophosphate doped with the Eu^{3+} and Eu^{2+} ions, *J. Alloys Compd.*, 2022, **896**, 163076.

64 H. Zhang, C. Hub, Y. Ding and Y. Lin, Synthesis of 1D Sb_2S_3 nanostructures and its application in visible-light-driven photodegradation for MO, *J. Alloys Compd.*, 2015, **625**, 90–94.